Spreading fronts and fluctuations in sedimentation

Laurence Bergougnoux, Sébastien Ghicini, and Élisabeth Guazzelli
Institut Universitaire des Systèmes Thermiques Industriels—CNRS UMR 6595, Polytech'Marseille, Technopôle de Château-Gombert, 13453 Marseille Cedex 13, France

John Hinch
Department of Applied Mathematics and Theoretical Physics, University of Cambridge, Silver Street, Cambridge CB3 9EW, United Kingdom

(Received 22 October 2002; accepted 9 April 2003; published 5 June 2003)

A diffuse interface or ''front'' at the top of the suspension is investigated experimentally and numerically. The width of the front is found to grow linearly in time, mainly due to a polydispersity of particle size in the very dilute experiments, and due only to fluctuations in particle density in the simulations. Away from the front, the fluctuations in the particle velocities are found not to decay. © *2003 American Institute of Physics.* [DOI: 10.1063/1.1578486]

I. INTRODUCTION

While the average velocity of a suspension of spheres sedimenting in a viscous fluid can be successfully predicted theoretically,[1] we are still unable to predict the root-mean-square fluctuations. Theories[2,3] and numerical computations with randomly positioned particles and periodic boundary conditions[4–7] find that the fluctuations diverge with the size L of the container as $V_S\phi^{1/2}(L/a)^{1/2}$, where V_S is the fall speed of an isolated sphere of radius a and ϕ is the volume fraction.

Unfortunately experiments find differently. At a moderate concentration of 5% and using particle tracking, Nicolai and Guazzelli[8] found that the fluctuations were the same for three different sizes of container. At very low concentrations and measuring depth-average velocity by particle image velocimetry (PIV), Segrè, Herbolzheimer, and Chaikin[9] found a $V_S\phi^{1/3}$ dependence, and an independence of the cell width if it exceeded a correlation length $\approx 20a\phi^{-1/3}$. However, for the major part of their experiments, this observed correlation length was of the same order as the cell depth. The dependence on the cell width was also recently questioned by Bernard-Michel *et al.*[10] using a very small square cell. At very low concentration and using PIV with a thin laser-sheet, Guazzelli[11] observed large vortices of the size of the cell width which decrease with time to reach a size of $\approx 20a\phi^{-1/3}$, smaller than the width of the square container. Velocity fluctuations seem also to reach a steady state. But this requires confirmation and so does the scaling of the observed steady correlation length.

There have been a number of theoretical papers attempting to explain this screening of the fluctuations.[12–16] One theoretical way out, proposed by Luke,[16] is that a vertical gradient in the mean concentration would suppress fluctuations so they would no longer depend on the size of the container but on the stratification assumed. Also, recent numerical simulations[17] for moderate volume fractions and nonvanishing small Reynolds number show that a container bottom is necessary to obtain saturation of the velocity fluctuations.

Recent experiments and numerical simulations by Tee *et al.*[18] and Mucha and Brenner[19] have observed a very interesting diffuse interface between the suspension and the clear fluid. They propose a theoretical model based on the idea of the effect of stratification proposed by Luke.[16] The main argument is that a very small vertical stratification caused by the broadening of the sedimenting front can change the characteristics of the velocity fluctuations.

There have been previous experimental investigations of the diffuse sedimentation front[20–22] that showed the importance of hydrodynamic dispersion, polydispersity of the particles, and hindered settling effects. Early times seem to be controlled by hydrodynamic dispersion and the fronts can grow diffusively with the square root of time. Later the effect of polydispersity dominates and the fronts can grow linearly in time. Eventually, hindered settling effects lead to an equilibrium thickness.

In this paper, we examine both by laboratory experiments and numerical simulations how the sedimentation front spreads and how this affects the fluctuations.

II. EXPERIMENTAL TECHNIQUES

A. Particles and fluid

The particles were glass spheres with a large index of refraction of 1.8 supplied by Cataphote. The particle size distribution was analyzed by using a (768×512 pixels) CCD camera and a digital imaging system composed of an acquisition board and of the public-domain image-processing NIH Image developed at the U.S. National Institute of Health. From measurements of the projected bead surfaces, the particle-radius distribution was found to be approximately Gaussian with a mean particle radius $\langle a\rangle = 149$ μm and a standard deviation of 8 μm. The particle density was determined by measuring the volume variation when a weighted amount of particles was introduced into a known volume of distilled water in a graduated vessel. The particle density was $\rho_p = 4.11 \pm 0.07$ gcm^{-3}.

The suspending fluid was silicon oil 47*V*1000 which had an index of refraction of 1.4, a viscosity $\mu = 10.0 \pm 0.3$ P,

and a density $\rho_f = 0.965 \pm 0.007$ gcm^{-3} at the air-conditioned room temperature of 25 ± 1 °C.

For this combination of fluid and spheres, the Stokes' velocity of an isolated sphere calculated with the Stokes' formula, $V_S = 2(\rho_p - \rho_f)\langle a \rangle^2 g/9\mu$ (where g is the acceleration due to gravity), was 0.015 ± 0.002 cm/s (the error bar estimated by computing the usual propagation of error in formula is mainly due to particle size dispersion). The sphere Reynolds number, $\langle a \rangle V_S \rho/\mu$, was smaller than 10^{-4} and the Brownian Péclet number was very large.

B. Experimental procedure

Experiments were performed in a glass walled cell of square cross section 20×20 cm^2 with a filled height of 40 cm. The particle volume fraction of the suspension was kept constant at $\phi = 0.300\% \pm 0.003\%$ for all the experiments. The cell width, L, and height, H, were then large compared to the particle radius, $\langle a \rangle$, and to the mean interparticle spacing, $\langle a \rangle \phi^{-1/3} \approx 0.1$ cm: $L \approx 1342\langle a \rangle \approx 194\langle a \rangle \phi^{-1/3}$ and $H \approx 2685\langle a \rangle \approx 387\langle a \rangle \phi^{-1/3}$. During the experiments, the cell was held in a fixed position on a rail, with the cell walls oriented vertically within 0.05 cm. The CCD camera was fixed on the same rail in front of the cell and could slide vertically.

Each sedimentation experiment consisted of mixing the suspension with a small propeller fixed at the end of a shaft driven by a variable-speed drill motor. The propeller was moved randomly within the suspension for several minutes in order to obtain a visually uniform particle distribution throughout the suspension. Caution was taken not to entrain too many air bubbles through the liquid–air interface, which in a viscous liquid take a long time to rise to the surface, during which time they create large velocity fluctuations. The starting time of each experimental run ($t = 0$) corresponded to the cessation of mixing. Two types of experimental measurements were then performed. The spreading of the sedimentation front was measured using the attenuation of light through the suspension. The particle velocities were measured using particle image velocimetry (PIV).

C. Light attenuation technique

The light attenuation was measured with the camera and the digital imaging system. The cell was back-lit by using two neon tubes. Sheets of tracing papers were placed between the neon tubes and the back of the cell in order to obtain a lighting as homogeneous as possible and sheets of black paper were placed on the side of the cell in order to avoid lateral light. A centered cross-section of the cell of 13×9.5 cm located at different positions from the top of the liquid–air interface was imaged by the camera. The video output of the camera was set to be linearly proportional to the received light quantity.

We first established the calibration law giving the light attenuation received by the camera at a given location along the cell as a function of the mean particle volume fraction ϕ. The gray level averaged intensity of all the pixels of the image, I, was recorded at a given volume fraction just after the cessation of the mixing of the suspension. The same measurement was performed through the pure fluid and yielded the intensity, I_0, for zero particle volume fraction. The attenuation of the light, defined by I/I_0, was found to be a monotonically decreasing function of the mean volume fraction ϕ with a best fitting law: $\ln(I/I_0) = -1.9\phi^{0.9}$ for $0 \leqslant \phi \leqslant 0.3\%$. Owing to the good homogeneity of the backlighting of the cell, the same calibration laws were obtained at different locations along the cell (with the top of the imaging windows being located at 5, 17, and 27 cm below the top of the liquid–air interface).

Using this calibration law, we could then determine the variation of the volume fraction $\phi(t)$ with time t at different heights, ζ, measured from the location of the liquid–air interface. The 13×9.5 cm imaging window was positioned at 0, 5, 17, and 27 cm below the top of the liquid–air interface. At each location, a series of images separated by 60 seconds was acquired by the camera to record the evolution of the moving sedimentation front. The averaged intensity of each pixel row of the image was recorded as a function of time. This gave the intensity of the transmitted light, $I(t)$, at a given height ζ. In order to determine the variation of the volume fraction, $\phi(t)$, an image of the pure fluid was also acquired by the camera and used to provide the reference intensity, I_0, in the calibration law.

This technique has been merely used to infer the particle concentration from the amount of light attenuation by particles. It is however important for the discussion of the experimental results to examine what exact quantity the technique is probing. It is certainly not the size of the particles. We can consider here that, since the index of the particles differs from that of the fluid, the light attenuation is mainly due to light scattering by the surfaces of the spheres; see for instance, Ref. 23. In addition, we can expect that the effect of multiple scattering is probably small at the low volume fraction used in the experiment.

D. Particle image velocimetry

We used a thin light-sheet of thickness ≈ 1 mm produced by two 15 mW laser diodes facing each other to illuminate the median plane of the cell. The camera placed in front of the cell and perpendicular to the light-sheet was focused on the illuminated particles which scattered the light. The centered imaging window was located at 25.5 cm below the liquid–air interface. A large imaging window of 19.0×13.4 cm^2 nearly covering the whole width of the cell was first used. Then, in a second set of experiments, the window was zoomed to 6.0×4.2 cm^2 in order to increase the spatial resolution.

In a typical experiment, a series of pairs of images was acquired using the digital imaging system. Successive pairs were separated in time by 60 seconds and the two images in a pair by one second (approximately one Stokes' time, $t_S = \langle a \rangle / V_S$). The pairs were then processed to find the velocity-vector map of the flow field by using an adapted source code and compiled application for PIV developed by Cardoso.[24]

The PIV technique is based upon the cross-correlation of the gray levels of a pair of images. This requires each image

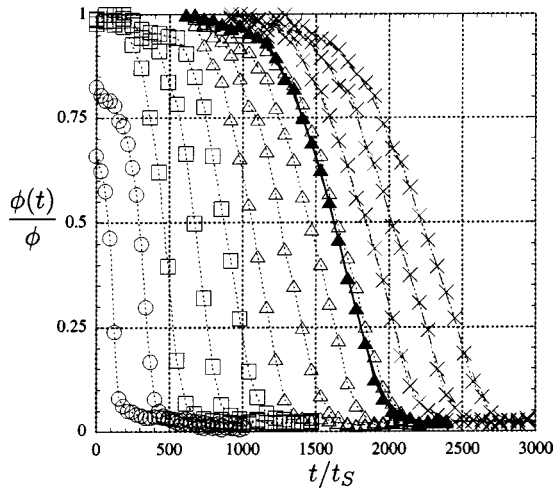

FIG. 1. Evolution of the concentration profile $\phi(t)/\phi$ versus dimensionless time, t/t_S, at different heights $\zeta=2,5,8,11,14,17,20,23,26,29,32,35$ cm. The concentration profile for $\zeta=25.5$ cm is represented by ▲. The data coming from measurements at different locations of the imaging window are differentiated by different symbols: ○, □, △, × for window positioned at 0, 5, 17, and 27 cm, respectively.

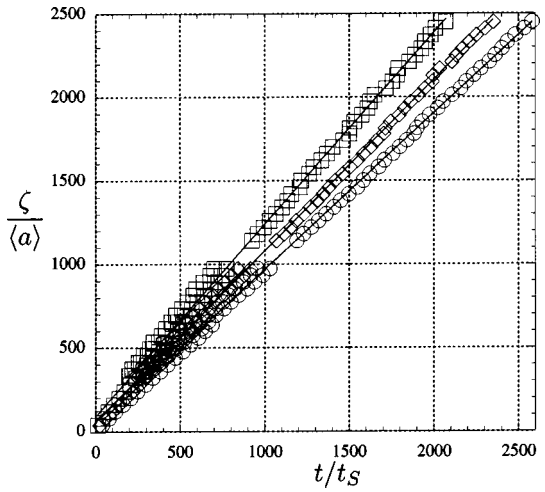

FIG. 2. Dimensionless falling distance, $\zeta/\langle a\rangle$, versus time (in unit of t_S) for the first (○), median (◇), and third (□) quartiles. The different lines indicate the best linear fits.

first to be discretized into a map of 33×33 nodes. Then, in a small interrogation region explored around each node, the local particle displacement between the two images is measured using direct cross-correlation.

This is repeated around each node to build up the complete two-dimensional velocity-vector field, u in the horizontal direction x and w in the vertical direction z. Velocity fluctuations, u' in the x direction and w' in the z direction, are found by subtracting the mean.

The spatial resolution of the measurement in the median plane of the cell is determined by the size of the interrogation region which is 108×108 pixels^2 ($\approx2.7\times2.8$ cm^2 for the large imaging window and $\approx0.84\times0.89$ cm^2 for the zoomed window) in order to contain enough particles to obtain reliable measurements. In the cell-depth direction, the measurement probes a thin layer $\approx6\langle a\rangle$ corresponding to the thickness of the light-sheet such as in the previous PIV experiments of Guazzelli[11] and Bernard-Michel *et al.*[10] This differs from the PIV measurements of Segrè *et al.*[9] and Tee *et al.*[18] where particles are imaged across the entire cell-depth, which reduces the apparent velocity fluctuations when the correlation length is smaller than the cell depth.

III. EXPERIMENTAL RESULTS

A. Sedimentation front

The evolution of the sedimenting front as a function of time is presented for different heights, ζ, measured from the top of the liquid-air interface in Fig. 1. At any given intermediate volume fraction, the curves coming from equispaced heights are equally spaced in time, meaning that a particular concentration is varying roughly at constant velocity. Because the spacing in time is less for the higher concentrations, the width of the front is growing in time, roughly linearly.

To obtain a better measurement of the spreading of the front, we have followed the approach of Davis and Hassen.[20] The data can indeed be used to determine the interface median time, $t_{1/2}$, as well as the first and third quartile times, $t_{1/4}$ and $t_{3/4}$, corresponding to the time taken by the iso-concentration planes at $\phi(t)/\phi=1/2$, 1/4, and 3/4, respectively, to fall a distance ζ. The falling distance is plotted versus these different times in Fig. 2. There is a clear linear increase with time. The slopes of these lines correspond to the average velocities of the iso-concentration planes at $\phi(t)/\phi=1/2$, 1/4, and 3/4. Table I gives the first quartile, median, and third quartile velocities of the interface, $w_{1/4}$, $w_{1/2}$, and $w_{3/4}$, found by using linear fits with correlation coefficients of 0.99.

Another convenient way of analyzing these data, also taken from Davis and Hassen,[20] is to plot the quartile interface thickness, $\delta=t_{1/2}(\zeta/t_{3/4}-\zeta/t_{1/4})$, as a function of the falling distance, ζ, as displayed in Fig. 3. This plot shows again that the interface thickness increases linearly with the settling distance. The relative quartile interface thickness, δ/ζ, is given by the slope of the line ≈0.20 in Table I (the correlation coefficient of the linear fit of 0.99).

In Figs. 1 and 3, we have also differentiated the data coming from measurements at different locations of the imaging window. The data collected in the window positioned at the top of the air–fluid interface (○) are slightly below the linear fit in Fig. 3. This discrepancy lies in the difficulty of

TABLE I. Dimensionless first quartile, median, and third quartile velocities of the interface, $w_{1/4}/V_S$, $w_{1/2}/V_S$, and $w_{3/4}/V_S$, respectively, and relative interface thickness, δ/ζ, deduced from the experimental data and from predictions accounting for polydispersity by considering that the light attenuation technique probes the surface of the particles.

	Experiment	Prediction
$w_{1/4}/V_S$	0.94	0.94
$w_{1/2}/V_S$	1.03	1.00
$w_{3/4}/V_S$	1.15	1.09
δ/ζ	0.20	0.15

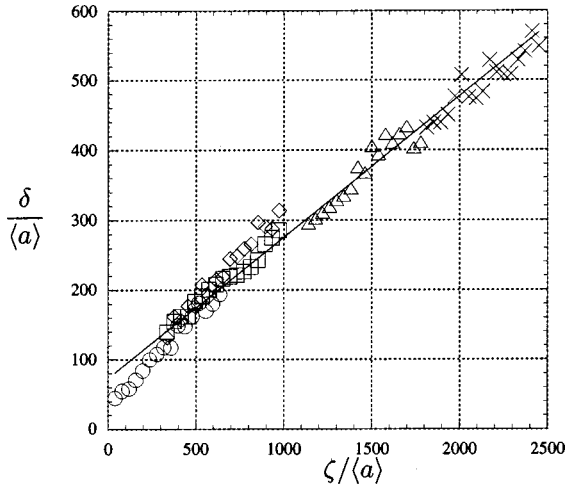

FIG. 3. Dimensionless quartile interface, $\delta/\langle a \rangle$ versus dimensionless falling distance, $\zeta/\langle a \rangle$. The symbols indicate the different locations of the imaging window at 0 (○), 5 (□ and ◇), 17 (△), and 27 cm (×) from the top of the liquid–air interface. The line indicates the best linear fit. The data coming from measurements at different locations of the imaging window are differentiated by different symbols: ○, □ and ◇, △, × for window positioned at 0, 5, 17, and 27 cm, respectively.

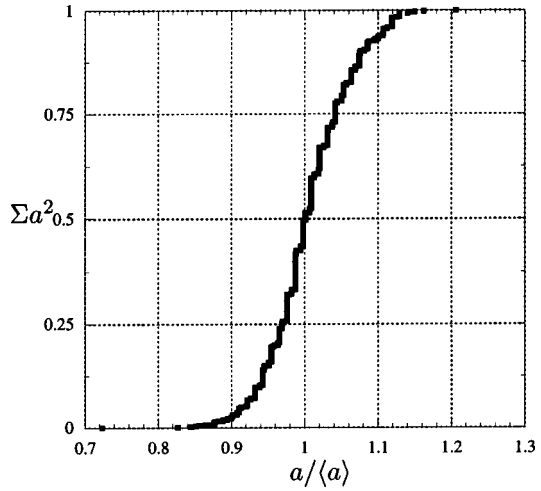

FIG. 4. Normalized cumulative sum of the square of the radius, a^2, versus dimensionless radius, $a/\langle a \rangle$.

performing a perfect uniform mixing at the very top of the suspension without entraining any air bubbles. This produces a mean concentration slightly lower than the expected $\phi = 0.3\%$ as can be seen in Fig. 1. These earlier time data may also be affected by hydrodynamic dispersion, although the dispersion coefficient is very small at the low volume fraction used here.[20,21] A linear regression excluding these data gives a relative quartile interface thickness $\delta/\zeta \approx 0.19$. In Fig. 3, we have also reported two different sets of data coming from two experiments performed at the same window location (□ and ◇) in order to show the sensitivity of the light attenuation technique for a good determination of the reference intensity. There was indeed difficulty in determining the correct reference intensity for the data represented by the ◇ which lie slightly above the linear fit. The other data (△ and ×) taken in lower window locations show an excellent linear increase.

It is possible at this point to examine whether the above linear spreading of the interface can be accounted for by the polydispersity in particle size. It should be noted first that, at the very small volume fraction $\phi = 0.3\%$, the self-sharpening of the interface caused by hindered-settling effects can be neglected (the hindrance is $\approx 1.5\%$). In this limit of very low volume fraction, the spreading of the interface can then be predicted by considering that the light attenuation technique probes the surface of the polydisperse particles.

From the measured particle-radius distribution, we can infer the distributions of the square of the radius a. The cumulated distribution of the square of the radius is shown in Fig. 4. We can then deduce the first quartile, median, and third quartile radii, $a_{1/4} = 0.970\langle a \rangle$, $a_{1/2} = 1.001\langle a \rangle$, and $a_{3/4} = 1.042\langle a \rangle$, respectively. The predicted quartile interface thickness, $\delta/\zeta = (a_{3/4}^2 - a_{1/4}^2)/a_{1/2}^2$, is given in Table I. The experimental thickness is much greater than this prediction. The polydispersity can only account for 75% of the linear spreading.

A slightly refined examination of this discrepancy can be obtained by estimating the first quartile, median, and third quartile velocities due to polydispersity. These velocities are simply given by the Stokes' velocity computed for the first quartile, median, and third quartile radius and are presented in Table I. The experimental first quartile velocity is in rather good agreement with that predicted. But disagreement occurs for the average velocities of the denser isoconcentration planes. The experimental third quartile velocity is 5% larger than the prediction.

It would be interesting to study further the unexplained 25% of the spreading of the front. Unfortunately, having substracted off the 75% due to polydispersity, we are left with a small quantity susceptible to large experimental uncertainty. Further we do not know how to deconvolve the simultaneous actions of polydispersity and other effects such as hydrodynamic dispersion.

B. Velocity fluctuations

Figure 5 displays typical velocity-fluctuation fields as sedimentation proceeds measured with the large imaging window of 19.0×13.4 cm^2 located at 25.5 cm from the top air–liquid interface. The initial mixing process creates uncorrelated velocities which vanish within a few Stokes' times. A spatially correlated structure, or vortex structure, of the size of the cell quickly emerges ($t/t_S = 10$). This vortex structure diminishes in size and strength with time and the velocity field becomes a complex three-dimensional structure composed of smaller vortices ($t/t_S = 135$, 571, and 945), as previously observed by Guazzelli.[11]

Velocities, u and w, and the square velocity fluctuations, u'^2 and w'^2, were ensemble-averaged over 9 runs taken at the same time after the cessation of mixing. It should be noted that computing the variance of the velocity for all runs gives the same results as computing the ensemble average of the square of the velocity fluctuations.

The mean horizontal velocity, $\langle u \rangle$, was always found to

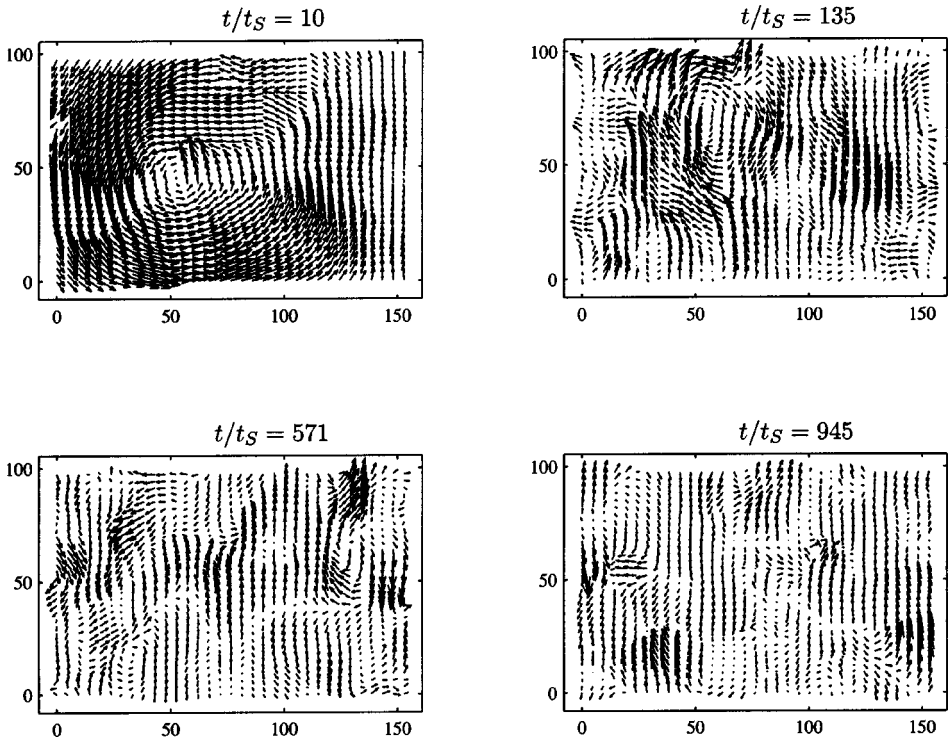

FIG. 5. Velocity-fluctuation fields across nearly the whole cell-width (large imaging window of 19.0 $\times 13.4$ cm^2) during the sedimentation process. Distance is plotted in mean interparticle spacing, $\langle a \rangle \phi^{-1/3}$. The vectors have been automatically scaled to prevent them from overlapping and then multiplied by a factor of 3.

be zero within error bars. The mean vertical velocity, $\langle w \rangle$, and the vertical velocity fluctuations $\langle w'^2 \rangle^{1/2}$, are plotted as a function of time in Fig. 6. After an initial transient, the mean velocity is V_S within error bars. It then starts to decrease at $t/t_S \approx 1000$ when the sedimenting front reaches the top of the imaging window thus leaving smaller slower particles behind. The concentration profile for $\zeta = 25.5$ cm (▲) in Fig. 1 shows that the sedimentation front reaches this location at $t/t_S \approx 1000$, nearly half of the front has passed through it at $t/t_S \approx 1500$ and most of the front at $t/t_S \approx 2000$. The velocity fluctuations are large $\approx 2.5 V_S$ at early times, and then, decrease to a uniform value $\approx 0.5 V_S$ at $t \approx 300 t_S$. A much smaller decrease (from 0.5 to $0.4 V_S$) is experienced for $t/t_S \geqslant 1000$ when the sedimentation front has reached the top of the imaging window. The behavior of the horizontal velocity fluctuations, $\langle u'^2 \rangle^{1/2}$, is similar. They reach a uniform value $\approx 0.25 V_S$ at $t \approx 300 t_S$.

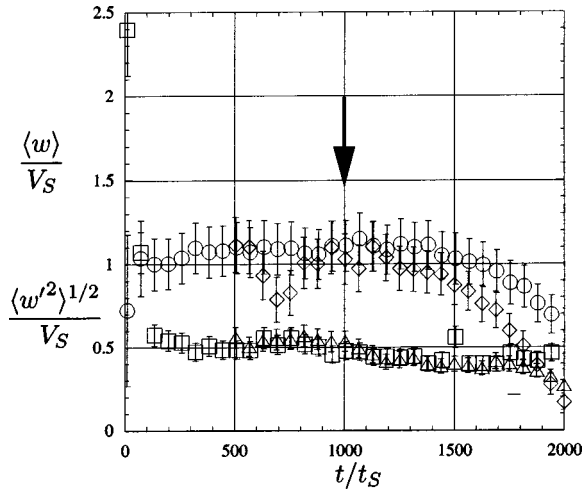

FIG. 6. Dimensionless mean vertical velocity, $\langle w \rangle / V_S$ (○ with the large imaging window and ◇ with the zoomed window), and velocity fluctuations $\langle w'^2 \rangle^{1/2} / V_S$ (□ with the large imaging window and △ with the zoomed window), versus dimensionless time, t/t_S. The arrow indicates when the sedimentation front reaches the top of the imaging window.

To detect more accurately the spatial-correlation of the smaller vortices, we have also performed experiments with a zoomed window 6.0×4.2 cm^2 at the same location from the top. In the steady-state regime before the front reaches the top of the window ($300 < t/t_S < 1000$), the values of the mean velocity and the velocity fluctuations are found to be the same within error bars as those measured with the large window (see Fig. 6). The decrease due to the sedimenting front ($t/t_S \geqslant 1000$) is slightly stronger because the averaging is performed on a smaller scale within the front.

To understand how the large initial vortex decreases in size and strength with time and whether an ultimate size is reached before the front arrives, we computed the spatial correlation in velocity fluctuations, for instance $C_z(x) = \langle w'(x_0) w'(x_0 + x) \rangle$, ensemble averaged over different starting positions x_0 on the velocity map and the different runs, as well as the power spectrum of the velocity fluctuations ensemble average over the different runs.

The behavior of the normalized correlation-function of the horizontal velocity-fluctuations along the horizontal direction, $C_z(x)/C_z(0)$, is analyzed at different times after the cessation of mixing in Fig. 7. When this function goes through a negative minimum, this indicates that the velocities are anti-correlated. The location of the minimum gives an estimate of the size of the vortex, or correlation length. At $t/t_S = 10$, the negative amplitude is large and the correlation length is $\approx L/2$; see Fig. 7(a). As time is increased, the amplitude of the minimum decreases and so does the correlation

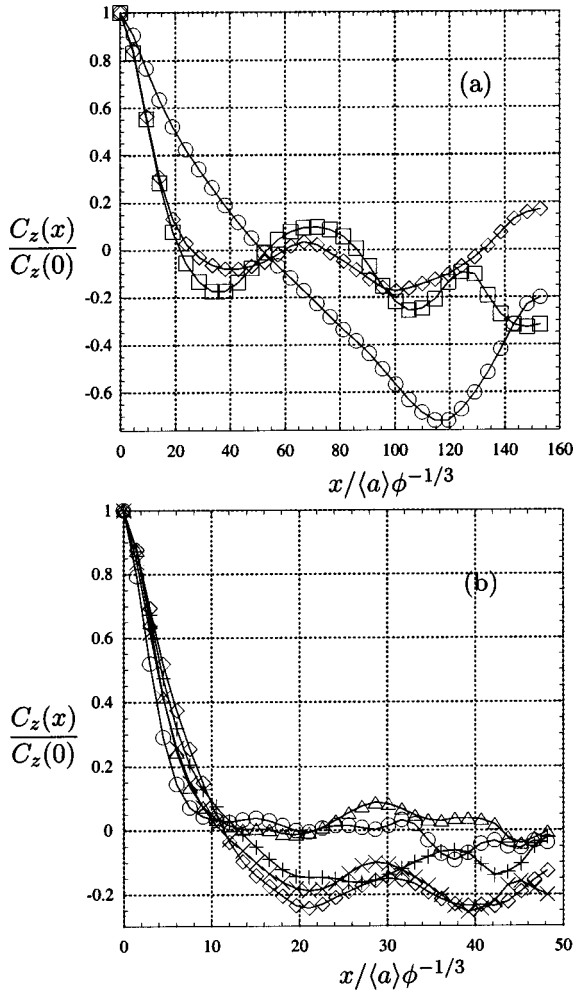

FIG. 7. Normalized spatial correlation function of the vertical velocity fluctuations, $C_z(x)/C_z(0)$, along the dimensionless horizontal direction, $x/\langle a\rangle\phi^{-1/3}$, at (a) $t/t_S=10$ (○), 197 (□), 446 (◇), with the large imaging window, and at (b) $t/t_S=504$ (×), 691 (+), 878 (◇), 1127 (△), 1933 (○), with the zoomed window.

length. In the uniform regime of velocity ($300<t/t_S<1000$), $C_z(x)/C_z(0)$ no longer seems to vary and the correlation length is $\approx 20\langle a\rangle\phi^{-1/3}$ (≈ 2 cm, which is larger than the spatial resolution of the zoomed imaging window ≈ 0.84 cm); see Fig. 7(b). These results confirm the observation of Guazzelli.[11] Of course a wider range of ϕ would need to be studied to validate the exact scaling of the correlation length. In addition, we find that, in the sedimentation front, $t/t_S \geqslant 1000$, velocity correlation is eventually lost; see again Fig. 7(b).

The power spectrum displays a broad peak at low frequencies which decreases and becomes quickly buried by noise with increasing time. In Fig. 8, we have plotted the relative magnitude of the largest first mode (of length ≈ 15.8 cm in the horizontal direction and ≈ 10.1 cm in the vertical direction) of the power spectrum of the horizontal and vertical velocity fluctuations projected in the horizontal and vertical direction as a function of time. By fitting the rapid first decrease by an exponential law, we find a decay time $\approx 40-60t_S$. This gives a crude estimate of the decay time of the velocity amplitude of the large initial vortex

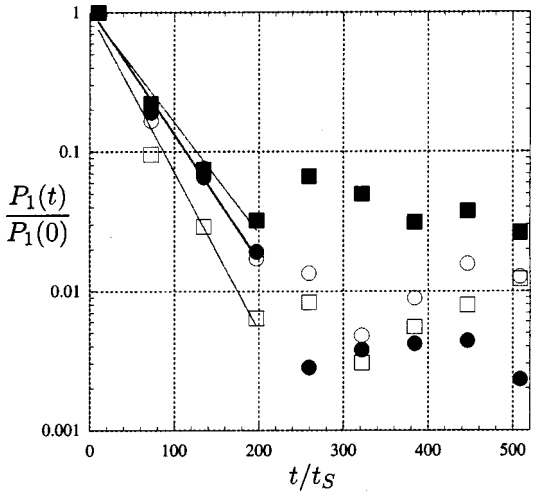

FIG. 8. Relative magnitude of the largest first mode of the power spectrum, $P_1(t)/P_1(0)$, of the horizontal and vertical velocity fluctuations projected in the horizontal (● and ■, respectively) and vertical (○ and □, respectively) directions as a function of dimensionless time, t/t_S. The different lines indicate the best exponential fits.

$\approx 80-120t_S$. We can then say that the initial vortex (of size $L/2$ and velocity $2.5V_S$) roughly makes 1/8 of a turn before it vanishes. This happens well before the arrival of the front in our experiments.

IV. COMPUTER SIMULATIONS

Some simplified simulations have been made of particles sedimenting in a very dilute suspension. Computer simulations compliment laboratory experiments with advantages and disadvantages. On the positive side, effects of polydispersity can be eliminated, the initial condition can be made well-mixed before gravity is turned on, many more realizations can be made for improved statistics, and certain quantities of interest such as density fluctuations can be easily measured. On the negative side, the number of particles in simulations will always be very much smaller than in experiments, and the complex long-ranged multi-particle hydrodynamics interactions must be severely simplified.

For the simulations of a very dilute suspension in this paper, the hydrodynamic interactions have been simplified in a way which represents well the large-scale cooperative motions on the scale of the container at the expense of poorly representing flows on the scale of the particles, with the divide between large and small scale being the inter-particle separation.

We consider N particles in a box $L\times L\times H$, where the height H is larger than the width L, typically $H/L=6$ or 10. The particles have radius a and weight mg (compensated for buoyancy) and move in a viscous fluid (negligible inertia) of viscosity μ. The volume fraction of particles $\phi=N(4\pi/3)a^3/L^2H$ is taken to be very small. The Stokes settling velocity for an isolated particle (assumed spherical) is $V_S=mg/6\pi\mu a$. The simulations are non-dimensionalized for the large-scale motions by scaling lengths with the width L and velocities with $mg/\mu L$. With these scalings, the non-

dimensional height is $h=H/L$ and the nondimensional Stokes settling velocity is $L/6\pi a$.

The large-scale motion induced by the particles is found as a superposition of a limited number of Fourier modes

$$\mathbf{u}(x,y,z)=\sum_{i=0}^{nx}\sum_{j=0}^{ny}\sum_{k=1}^{nz} u_{ijk} \times\left(\frac{ik}{h}\sin(\pi ix)\cos(\pi jy)\cos(\pi kz/h),\right.$$
$$\frac{jk}{h}\cos(\pi ix)\sin(\pi jy)\cos(\pi kz/h),$$
$$\left.-(i^2+j^2)\cos(\pi ix)\cos(\pi jy)\sin(\pi kz/h)\right).$$

These Fourier modes satisfy the incompressibility condition $\nabla\cdot\mathbf{u}=0$, and vanishing normal velocity on the side walls $x=0$ and 1 and $y=0$ and 1, and the bottom and top $z=0$ and h. On these boundaries, they do not satisfy the usual no-slip rigid boundary condition, but instead zero tangential stress, e.g., on the side walls $x=0$ and 1, $\mu(\partial u/\partial y+\partial v/\partial x)=0=\mu(\partial u/\partial z+\partial w/\partial x)$. The amplitude of the Fourier modes of the velocity are related to the Fourier modes of the density ρ_{ijk} by

$$u_{ijk}=\rho_{ijk}/\pi^2(i^2+j^2+k^2/h^2),$$

where the density amplitudes are found by summing over the weight of the point-like particles at (x_p,y_p,z_p)

$$\rho_{ijk}=\frac{8c_{ijk}}{h}\sum_{p=1}^{N}\cos(\pi ix_p)\cos(\pi jy_p)\sin(\pi kz_p/h),$$

with $c_{ijk}=1$ if neither i nor j vanish, 1/2 if one vanishes and 1/4 if both do. The number of Fourier modes was taken to be the same in each horizontal direction $ny=nx$, and higher in the vertical by the aspect ratio, $nz=h\,nx$, with nx varying between 5 and 12. The total number of Fourier modes was usually set equal to the total number of particles, i.e., $N=h\,nx^3$, with N varying between 750 and 10 368. This means that there are sufficient modes to resolve motions for the whole container down to the inter-particle separation $(h/N)^{1/3}$, which is much larger than the nondimensional size of the particle $a/L=(h/N)^{1/3}(3\phi/4\pi)^{1/3}$. Occasionally it was necessary to distinguish between the inter-particle separation $(h/N)^{1/3}$ and the smallest numerical resolution $1/nx$, and for this purpose the link $N=h\,nx^3$ was broken.

The above numerical method for finding the velocity of all the particles is essentially an N^2 method (N particles$\times N$ Fourier modes). However, the most expensive part is the evaluation of the $2(nx+ny+nz)$ trigonometric functions for each particle. By evaluating and storing these before using them, the computational time could be reduced by a factor nx^2.

The Fourier representation used in this paper for the flow induced by the particles is similar to that used recently by Mucha *et al.*[19] They had a computational cell with the horizontal breadth smaller than the horizontal width, reflecting the geometry of their laboratory experiment. They chose Fourier modes which satisfied the no-slip boundary condition on the front and back walls. The no-slip boundaries will reduce the magnitude of the induced velocities compared with the stress-free boundaries used in this paper, hopefully just by a constant numerical factor for the averaged quantities of interest. The no-slip modes are more complicated than the simple trigonometric functions used in this paper, entailing greater computational costs in their evaluation. Finally, Mucha *et al.*[19] used far fewer Fourier modes than number of particles, sometimes less than 1/100th.

The computations proceeded as follows. The particles were first positioned randomly within the cell. The induced flow at each particle was evaluated by the Fourier representation described above. The particles were then moved with this velocity using a second-order midpoint time–stepping method. (In retrospect, a second-order multi-step method with half the number of expensive velocity evaluations would have been better.) The size of the time–step was typically $\Delta t=0.01$, which is about half the shortest length-scale resolved, 0.1, divided by the largest velocity encountered, about 5. As the particles sediment, various statistics were collected. For each set of parameters, a number of realizations, typically 20, were made with different random initial positions of the particles.

It should be noted that the particle were moved only with the induced fluid flow and that other forces, such as excluded-volume forces, were excluded. The particles are effectively point-particles, so that the issue of overlap of particles cannot arise. The one exception was the occasional escape of a particle across the bottom boundary when the time–step was too large. Whenever this happened, the rogue particle was repositioned just above the bottom. Also it should be noted that there is no ''back-flow'' or ''hindered-settling'' effect in the simulations, because the effective volume fraction is zero for the point-like particles.

V. NUMERICAL RESULTS

A. Mean velocity

The mean settling velocity in the simulations is not the Stokes velocity, because the truncated Fourier representation cannot resolve the small radius of the effectively point-particles. The shortest length-scale resolved is $1/nx$, and this length in the Stokes drag leads to a nondimensional settling velocity $O(nx)$ (dimensional velocity $nx\,mg/\mu L$). For the initially random positions of the particles, the mean settling speed is at $t=0$

$$\langle w\rangle=-\frac{1}{\pi^2 h}\sum_{i=0}^{nx}\sum_{j=0}^{nx}\sum_{k=1}^{h\,nx}\frac{i^2+j^2}{(i^2+j^2+k^2/h^2)^2},$$

which is about $-0.147nx$, depending on the values of nx and h, the dominant contribution coming from the larger values of i, j, and k.

It would be possible to modify the simulations to have the correct mean settling velocity, by adding $-L/6\pi a+0.147nx$ to the induced flow at each particle. One would then also have to stop particles falling through the bottom

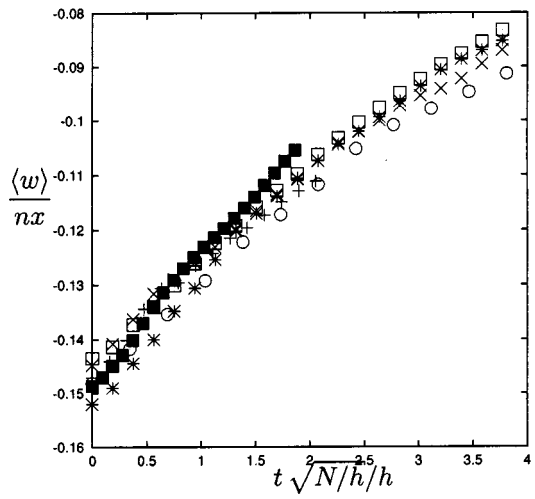

FIG. 9. The decrease of the mean settling velocity $\langle w \rangle$ scaled with the number of Fourier modes nx as a function of time t scaled with the time to fall the height of the container h at the rms velocity $\sqrt{N/h}$, where N/h is the number of particles per unit height. Averages are taken over all the particles in the simulation including the sediment, and are taken over about 20 realizations with different random initial conditions. The values of the parameters N,h,nx are, respectively: $\times$ 3072, 6, 8; $*$ 3072, 6, 5; □ 3072, 6, 12; ■ 750, 6, 5; ⊙ 10 368, 6, 12, and + 10 000, 10, 10.

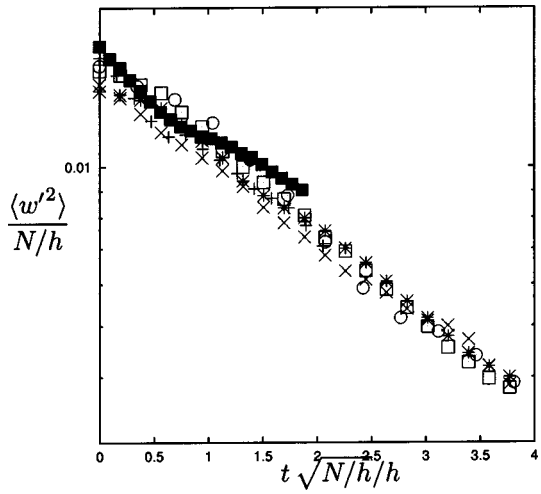

FIG. 10. The decrease of the variance of the velocity fluctuations $\langle w'^2 \rangle$ scaled with the number of particles per unit height N/h as a function of time t scaled with the time to fall the height h at the rms velocity $\sqrt{N/h}$. Averages are taken over all the particles including those in the sediment and over about 20 realizations. The values of the parameters are as in Fig. 9.

boundary. These modifications were tried and then abandoned because they shortened the sedimentation time and seemed to change nothing else.

Figure 9 shows how the mean sedimentation velocity decreases in time. The mean is taken over all the particles including some in the near stationary sediment. Scaling the mean velocity with nx and time with $h\sqrt{h/N}$ is found to collapse all the results into a single curve. The variation with nx is tested by simulations with $h=6$ and $N=3072$ and $nx=5$ $*$, 8 $\times$ and 12 □. The variation with N is tested by $h=6$ and $nx=5$ with $N=750$ ■ and 3072 $*$; and by $h=6$ and $nx=12$ with $N=3072$ □ and 10 368 ⊙. Finally the variation with h is tested by the above cases with $h=6$ and simulations with $h=10$, $nx=10$ and $N=10\,000$ $+$. The scaling of time $h\sqrt{h/N}$ is clearly connected to the magnitude of the velocity fluctuations and will be discussed in the next subsection.

B. Velocity fluctuations

For the initially random positions of the particles, the variance in the vertical velocity of the particles is given at $t=0$ by

$$\langle w'^2 \rangle = \frac{N}{\pi^4 h^2} \sum_{i=0}^{nx} \sum_{j=0}^{nx} \sum_{k=1}^{h\,nx} \frac{(i^2+j^2)^2}{(i^2+j^2+k^2/h^2)^4},$$

which is about $0.014N/h$, depending on the values of nx and h, the dominant contribution coming from the smaller values of i,j and values of k up to $O(h)$. These velocity fluctuations thus correspond to convection cells which fill the width of the container and extend over a depth equal to the width, i.e., have a ''square'' geometry. The origin of the convection cells is, as argued in Hinch,[3] the imbalance in the weight of two sides. The number of particles within such a square-shaped convection cell would on average be N/h (the number per unit height), with an imbalance in weight of two sides statistically of order $\sqrt{N/h}$ (unit weight particles in the nondimensionalization). This imbalance drives velocity fluctuations of order $\sqrt{N/h}$ (again with the chosen nondimensionalization of lengths and velocities).

The nondimensional result for the initial velocity fluctuations

$$w' \approx 0.12\sqrt{N/h} \quad \text{at } t=0,$$

corresponds to a dimensional result

$$1.1V_S\sqrt{\phi L/a}.$$

The above coefficient of 1.1 for simulations in this paper with stress-free walls should be compared with the value of 0.48 obtained by Mucha for no-slip on all four sides of a squared-sectioned cell, and 0.79 for periodic boundary conditions by Cunha *et al.*[7] The increase of the velocity fluctuations with the size of the container is a direct consequence of the initial random positioning of the particles.

Figure 10 shows the decrease in the velocity fluctuations in time. Statistics are taken using all the particles, including some in the near stationary sediment. Scaling the variance of the velocity $\langle w'^2 \rangle$ with N/h and time t with $h\sqrt{h/N}$ is found to collapse all the results into a single curve. As in Fig. 9, parameters were varied to test the variation with N and h and invariance with nx. The timescale $h\sqrt{h/N}$ can now be understood as the time for a typical heavy blob of $\sqrt{N/h}$ excess particles to fall at velocity $\sqrt{N/h}$ through the h convection cells which fill the height of the container.

The velocity fluctuations are seen to decay exponentially over the range plotted in Fig. 10. Some longer simulations to $t=20h/\sqrt{N/h}$ found a slowing down of the exponential decay which could be approximated by $0.01\Sigma n^{-2}\exp(-t/2n)$. In the initial exponential decay, the velocity fluctuations w' decrease by a factor e^{-1} in the time

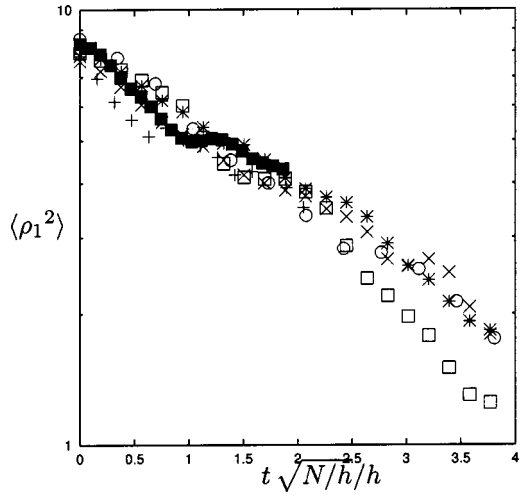

FIG. 11. The decrease of the group of the longest modes of the density fluctuations ρ_1^2 as function of time t scaled as in Figs. 9 and 10 with $h/\sqrt{N/h}$. The values of the parameters are as in Fig. 9.

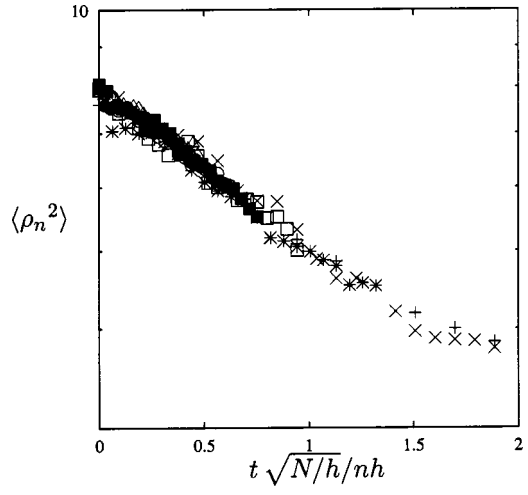

FIG. 12. The decrease of the groups of the density modes ρ_n^2 as function of time t scaled with $h/\sqrt{N/h}$. The results are for fixed $h=6$, $N=3072$ and $nx=8$, and with different $n=1$ +, 2 ×, 3 *, 4 □, 5 ■, 6 ⊙, 7 ●, and 8 △.

$t \approx 6/\sqrt{N/h}$. In this time a heavy blob would fall at $w' = 0.12\sqrt{N/h}$ through 3/4 of the height of the container.

C. Density fluctuations

The origin of the velocity fluctuations in the sedimentation is the random clumping of more particles on one side of the container compared with the other side. This statistical imbalance of weight drives strong convection cells. The basic imbalance can be measured by the Fourier amplitude of the density fluctuations ρ_{ijk} in the longest wavelengths, i.e., with i and $j=1$ and 0 and with $k=1,2,\ldots,h$ for "square" cells. Now for the initial random positions of the particles, the amplitude of each density mode is given at $t=0$ by

$$\langle \rho_{ijk}^2 \rangle = \frac{8 c_{ijk} N}{h^2},$$

where $c=1$ if neither i nor j vanish, 1/2 if one vanishes and 1/4 if both do. It is convenient to group together modes with similar wavelengths by defining for $n=1,2,\ldots,nx$

$$\rho_n^2 = \frac{h}{2Nh^2} \sum_{k=1}^{hn} \left(\sum_{\substack{j=n, 0 \le i \le n-1 \\ i=n, 0 \le j \le n}} c_{ijk} \rho_{ijk}^2 \right).$$

The initial value of each group amplitude is $\rho_n^2 = 8$.

Figure 11 shows the decrease in time of the longest mode of the density fluctuations, ρ_1^2. Scaling time as before with $h/\sqrt{N/h}$ collapses all the results into a single curve. As in Figs. 9 and 10, parameters were varied to test the dependence on h and N, and independence of nx. The longest density mode ρ_1^2 is seen to decay exponentially, at least over the range plotted. This mode drops by a factor e^{-1} in a time $t \approx 3/\sqrt{N/h}$, the same time over which the variance of the velocity fluctuations $\langle w'^2 \rangle$ drops by the same factor. The density fluctuations decay because the heavy clump of particles on one side of the container can fall at w' to the bottom in this time. With the heavy clump at the bottom, there is nothing to drive the convection cells, and so the velocity fluctuations decay.

Figure 12 shows the decay in time of all the groups of density modes ρ_n^2 $(n=1,2,\ldots,nx)$ for the one set of parameters $h=6$, $N=3072$, and $nx=8$. All the simulations with different values of the parameters gave the same results and so are not presented. Scaling time differently for each mode, with $nh/\sqrt{N/h}$, collapses the different modes onto a single curve. Thus the higher modes decay more slowly. Within the range plotted, the decay appears to be exponential

$$\rho_n^2(t) \approx 8 \exp\left(-\frac{\sqrt{N/h}}{3nh} t \right).$$

This simple form for the different modes inspired the approximate fit of the velocity fluctuations $0.01\Sigma n^{-2} \exp(-t/2n)$ quoted earlier.

No simple explanation can be offered for why the decay time of mode ρ_n^2 should be proportional to n. A square blob of size $1/n$ smaller than the width of the container in each direction would have n^{-3} less particle, and so density and velocity fluctuations $n^{-3/2}$ smaller. If such little blobs had to fall the full height of the container, they would take $n^{3/2}$ longer, not n longer. One can speculate that advection of such little blobs by the large-scale convections cells gives a nonlinear interaction between the different modes which invalidates the above reasoning.

D. Fronts

As a suspension sediments, the interface between the suspension and the clear fluid above can become diffuse. Such diffuse interfaces or fronts have been studied experimentally by several groups, but only recently seen in computer simulations, the simulations of Mucha *et al.*[19] In experiments, fronts can grow diffusively with the square roots of time due to hydrodynamic dispersion, can grow linearly in time due to polydispersity of the particles, and can tend to a steady thickness through the effects of back-flow or hindered settling. Computer simulations can suppress the experimental complication of polydispersity and, as in this paper, can suppress the hindered settling effects by a crude representation

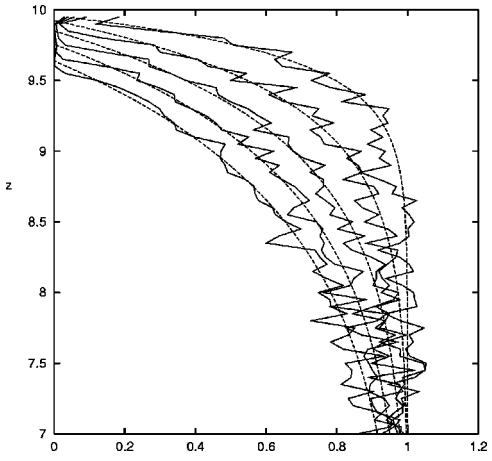

FIG. 13. Concentration profiles with height, normalized by the initial uniform value, at times $t=0.2$, 0.4, 0.6, 0.8, and 1.0, for parameters $h=10$, $N=10\,000$ and $nx=10$. The dashed curves are least-squared fits with an exponential function, giving thicknesses of the front between 25% and 75% of the full concentration as 0.32, 0.59, 0.83, 1.02, and 1.18, respectively.

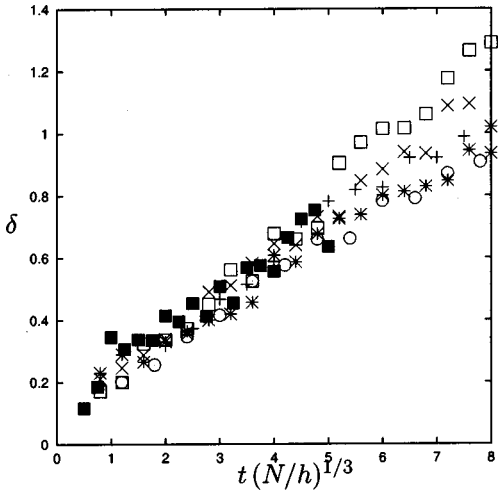

FIG. 14. The width of the front δ as a function of time scaled by the inter-particle spacing $(h/N)^{1/3}$. The values of the parameters are as in Fig. 9.

of the hydrodynamic interactions. It is not clear how the front would then grow, linearly or with the square root of time.

Concentration profiles with height were made during the simulations by binning the particles into layers of thickness $\Delta z=h/2nz$. These layers would contain on average $\frac{1}{2}nx^2$ particles, and so averages over at least 20 realizations are required to reduce the statistical noise to the 5% level.

Figure 13 gives the concentration profiles at the top of the suspension at time intervals of 0.2 up to $t=1.0$. The concentration has been normalized by the initial uniform value. One can see at any intermediate concentration that the curves equispaced in time are roughly equispaced in height, with greater displacements at larger concentrations. This indicates that the width of the front is growing roughly linearly in time.

E. Width of the fronts

To measure more precisely the width of the front, a least-squared fit to the concentration profile was made using a smooth function. A suitable simple function was found to be $1-e^{-\alpha(z-z_0)}$, without any theoretical suggestion for this particular form. The two parameters α and z_0 were selected to fit the concentration profile over the range $0.1\leqslant c\leqslant 0.9$. Following our experimental study described above, the width of the front δ was defined to be the height over which the concentration increased from 25% to 75% of the initial uniform value, thus $\delta=1.0896/\alpha$.

Figure 14 shows how the width of the front δ increases in time. All simulations have a linear grow in time over the range plotted. At later times, the front fills the entire height of the container, when it is difficult to define its width. At earlier times, there are insufficient number of bins involved to give an accurate measure of the width. Extrapolating back to $t=0$, the width would appear to be nonzero then, which may indicate an unresolved initial diffusion regime or may just be the limitations of the measurements of thin fronts.

Scaling time with the interparticle separation $(h/N)^{1/3}$ collapses all the different results onto a single curve. Parameters of the simulation were varied to demonstrate that the growth of the front did not depend on the height of the container h nor the number of Fourier modes nx. The linear growth in time is approximately

$$\delta\approx 0.12(h/N)^{1/3}t.$$

This nondimensional result corresponds to a dimensional growth

$$1.5\phi^{1/3}V_S t.$$

It is interesting to speculate on the dependence of the growth on the inter-particle separation $(h/N)^{1/3}$. Consider a cluster of particles of size ℓ. On average there will be $N\ell^3/h$ particles in the cluster, with statistical fluctuations $\pm\sqrt{N\ell^3/h}$ in the number. Consider a cluster which is heavier by such a statistical fluctuation. With the Stokes drag on the cluster being proportional to it size, it will fall faster than average by $w'=\sqrt{N\ell/h}$. Now the excess number will correspond to a local density fluctuation above the mean $\overline{\phi}$ by $\phi'=\overline{\phi}/\sqrt{N\ell^3/h}$. The faster fall of the heavy cluster therefore contributes to the flux of sedimenting particles by $\phi' w'=\overline{\phi}/\ell$. Thus the smallest clusters contribute the most, the size of the smallest identifiable cluster being the inter-particle separation $\ell=(h/N)^{1/3}$. As the heavier-than-average clusters fall faster, they leave behind the interface region depleted of particles, and so the width of the front grows. It should be noted that the width of the front in the simulations was much larger than the eddies the size of the inter-particle separation, except possibly at the first time measured, and this exceptional condition may explain the apparent failure of the width to vanish when extrapolated to $t=0$.

The above speculative argument suggests an additional flux of sedimenting particles proportional to $\phi^{4/3}$. If such a local flux-law could be applied to the diffuse interface, it would yield a so-called ''expansion fan'' growing linearly in time with a concentration profile $\phi(z,t)\propto[(z-z_0(t))/t]^3$. This cubic dependence is not found in the simulations, the

exponential form found having the opposite curvature. The $\phi^{4/3}$ flux-law may, therefore, be wrong, or alternatively its application to the front may be inappropriate without some hydrodynamic dispersion contributing to the flux.

The above examination of the growth of the front was motivated by the experimental findings, where polydispersity certainly gives a linear growth of the thickness in time. Without polydispersity, as in the simulations, one traditionally thinks in terms of the front growing through hydrodynamic dispersion. A constant diffusivity for hydrodynamic dispersion would give the thickness of the front growing with the square root of time. The data in Fig. 14 are not consistent with such a behavior. Recently, however, Mucha *et al.*[19] have proposed a model of the front in which stratification limits the size of the eddies, which leads to an interesting nonconstant hydrodynamic diffusivity. The hydrodynamic diffusivity is proportional to the size of the largest clusters ℓ and their velocity fluctuations w', i.e., $D=Kw'\ell$, where K is a constant to be determined. Now the velocity fluctuations are related through a Stokes drag to the number of extra particles in the cluster n', $w'=n'mg/\mu\ell$, while the number fluctuation is just the standard statistical fluctuation in the total number in the cluster, $n'=\sqrt{n\ell^3}$. Mucha *et al.* propose that the stratification $\partial n/\partial z$ would limit the size of the largest eddies when the effect of the stratification on the number in the cluster $\ell^3(\ell\,\partial n/\partial z)$ became as large as the statistical fluctuations $\sqrt{n\ell^3}$. This gives a maximum size of the cluster $\ell=n^{1/5}(\partial n/\partial z)^{-2/5}$ and so a diffusivity

$$D=K\frac{mg}{\mu}n^{4/5}\left(\frac{\partial n}{\partial z}\right)^{-3/5}.$$

Simple numerical solution of the nonlinear diffusion equation using this diffusivity shows a similarity form, with a shape which has very roughly $n\propto z^{1/3}$ up to the homogeneous value n_0, and with a thickness of the front, defined to be the distance over which the concentration increases from 25% to 75% of its homogeneous value

$$\delta=0.693\,n_0^{1/7}(Kmgt/\mu)^{5/7},$$

or $\delta=0.693\,(N/h)^{1/7}(Kt)^{5/7}$ in the non-dimensionalization used in our simulations.

In Fig. 15, we replot our numerical results for the thickness of the front as a function of $t^{5/7}(N/h)^{1/7}$. One sees again a good collapse of the data for this alternative theory, with no dependence on h and nx. The straight line corresponds to the constant of proportionality in the diffusivity $K=0.52$. Using the value, an alternative expression for the dimensional growth is

$$\delta/a=2.85\phi^{1/7}(V_st/a)^{5/7}.$$

Comparing the two Figs. 14 and 15, they equally seem to have no systematic variation with N/h. Further, they seem to be two equally good straight lines. Neither straight line goes exactly through the origin, but at early times the concentration changes over a vertical distance much smaller than the size of the largest clusters, and so smoothing by a continuum diffusion process is inappropriate. At present we do not have the data to distinguish between the two possible models. Moreover, it is possible that the two different physical processes of the two models act simultaneously.

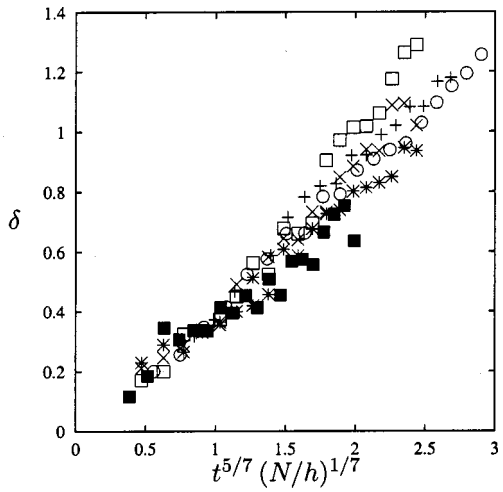

FIG. 15. The width of the front δ as predicted by the similarity solution of the nonlinear diffusion equation. The values of the parameters are as in Fig. 9.

F. Windowed samples

The results presented in the first three subsections, for the mean velocity and fluctuations in velocity and density, gathered statistics using all the particles in the simulation. This included some particles in the near stationary sediment and some in the large diffuse interface with the clear fluid above. Now wise to the existence of these special regions, an observation window was set on the simulations, rather similar to that standard in laboratory experiments, a window to exclude the special regions. For simulations with a height $h=6$, data were gathered from the window $2\leqslant z\leqslant 4$.

Figure 14 shows that the width of the front has increased to $\delta=1$ by time $t(N/h)^{1/3}=8$. This is the width of the region where the concentration varies between 25% and 75% of its initial uniform value. There are noticeable decreases in concentration at twice the width of the front, i.e., the front is arriving at the central observation window by the end of the simulations.

Figure 16(a) shows that the mean settling velocity within the central sampling window decreases in time by only 20%, while it roughly halved for the whole suspension in Fig. 9. Moreover for the first half of the period plotted in Fig. 16(a), the mean velocity hardly changes within the statistical noise (higher for the small window). Figure 16(b) for the decay of the velocity fluctuations shows again only small changes at early times, followed by a decrease by a reduced factor compared with observations for the whole suspension in Fig. 10. Clearly some of the large decays reported in the first three subsections are due to including particles in the sediment and in the front.

VI. CONCLUSIONS

In laboratory experiments and in numerical simulations, a large diffuse interface or front was observed between the

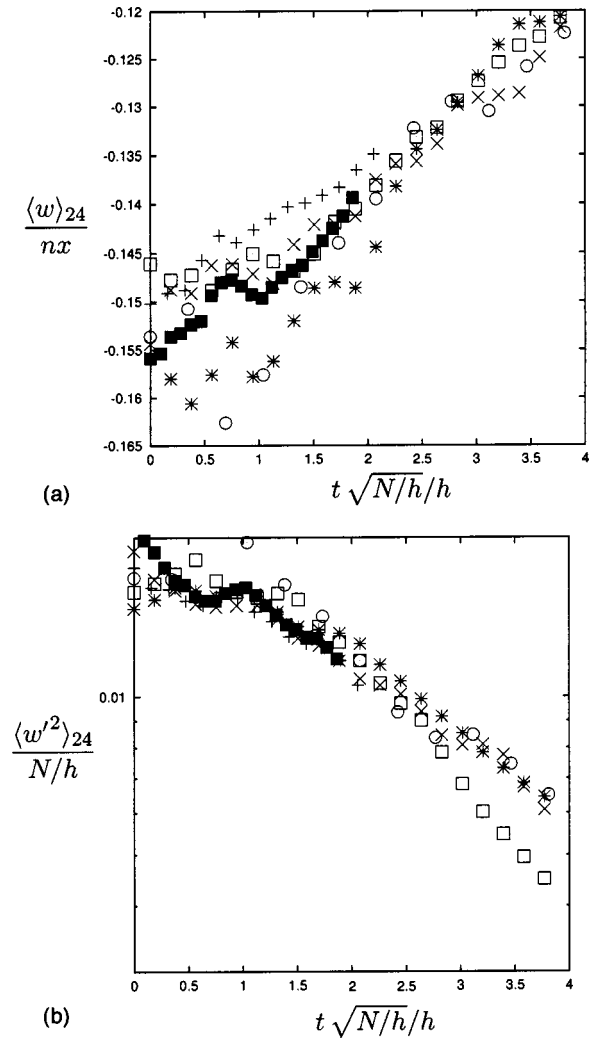

FIG. 16. Observations in a central sampling window $2 \leqslant z \leqslant 4$; (a) the mean settling velocity and (b) the variance of the velocity fluctuations. The values of the parameters are as in Fig. 9.

top of the suspension and the clear fluid above. In both experiments and simulations the width of the front seemed to grow linearly in time.

In the experiments, at very low concentrations $\phi = 0.3\%$, about three-quarters of the growth of $\delta = 0.20 V_S t$ could be explained by a polydispersity of the particle size. The extra growth comes from a faster fall of the denser isoconcentration planes. No diffusive growth, like the square root of time, due to hydrodynamic dispersion, can be seen in the plots that we have presented. It would be difficult to deconvolve the simultaneous actions of polydispersity and other small effects such as hydrodynamic dispersion or the enhancement to the flux from fluctuations, $\langle w' \phi' \rangle$. Hindered settling also played no role in the very dilute suspension.

The computer simulations excluded polydispersity and hindered settling, but also produced a large front growing in time. The numerical results fit equally well two different models. The first model has heavy clusters of the scale of the inter-particle separation falling faster leaving the interface region depleted of particles, which produces a linear growth in time of the thickness of the front, $\delta = 1.5 \phi^{1/3} V_S t$. When applied to the experiments with $\phi = 0.3\%$, this predicts a growth $\delta = 0.22 V_S t$, which a little larger than the $0.20 V_S t$ seen in the experiments, where three-quarters of the effect could be explained by polydispersity. The second model has a nonlinear hydrodynamic dispersion due to eddies whose size is limited by stratification, and has the thickness of the front growing according to $\delta/a = 2.85 \phi^{1/7} (V_S t/a)^{5/7}$. Applying this to the experiments with $\phi = 0.3\%$, predicts at $V_S t = 1250a$ a thickness $\delta/a = 203$ compared with the experimental value (including polydispersity) of 300 in the middle of Fig. 3. At this time, we do not have the data to distinguish between the two models.

A large front in a sedimenting suspension was reported by Tee *et al.*,[18] both in experiments and simulations. They did not study in detail the growth of the front in time. We are fairly certain that in their experiments there are important effects from polydispersity, which was greater than in our experiments, for their large particles, and Brownian motion for their small 3 μm particles.

The behavior of the particles is different in the front. In the experiments, we see the mean particle velocity and its fluctuations decrease as the front arrives in the observation window. Using a window which excluded the front and the sediment, the mean velocity remains constant near to the Stokes value and the fluctuations attain a steady value after an initial rapid transient. The velocity auto-correlation function similarly has a different form near the front, but in the bulk of the suspension quickly goes to a steady form. This steady form shows circulating eddies with a size about 20 inter-particle separations, as reported earlier by Segrè *et al.*[9] in thin cells and by Guazzelli[11] in square cell. It should be noted that the present experiments were at a single concentration and particle size and so have not tested the variation of the correlation length with $20a\phi^{-1/3}$.

In the simulations, the particle velocity fluctuations, along with the particle density fluctuations which are the origin of the velocity fluctuations, are found to decrease continually by orders of magnitude when the observations include all the particles, i.e., included the front and the sediment. Restricting observations to a region away for the large front and the sediment, the mean and fluctuations of the particle velocities remain roughly constant. As in all previous simulations, the magnitude of the initial velocity fluctuations depends on the size of the container, $w' \approx 1.1 V_S \sqrt{\phi L/a}$. Applied to the experiments with $\phi = 0.3\%$ and $L/a = 1342$, this predicts fluctuations $w' = 2.2 V_S$, which is comparable with the initial velocity fluctuations but four times larger than the steady experimental value. The simulations in this paper do use a very crude representation of the hydrodynamics, in particular stress-free walls which are expected to give velocities too large. It should also be noted that the width of the container in the simulations was always less than 20 inter-particle separations, the largest being 12 separations. However, there is no hint in the clear scalings of the results of

something special still to occur at 20 inter-particle separations. Finally it should be noted that the duration of the simulations was artificially prolonged by operating with the low mean settling velocity $0.147nx$ rather than the larger Stokes settling velocity, $L/6\pi a$ in the nondimensionalization used. Correcting this would leave the velocity fluctuations and spreading of the front unchanged, but would curtail the simulation earlier, and hence the velocity fluctuations would have decreased even less during the shortened simulation.

Different behavior of the particles in the front can be seen, we believe, in the experiments of Tee *et al.*[18] They observe a wide front the arrival of which in the measuring window may be the cause of the decrease of the velocity fluctuations. Noting that the polydispersity of their particles is larger than ours, we believe that their front will be a special region depleted of the larger heavier particles. We are, therefore, not surprised that they show different behavior of the particles when the front arrives.

To conclude, in agreement with Tee *et al.*[18] we have found a wide diffuse front in a very dilute sedimenting suspension. At higher concentrations, say higher than 1%, hindered settling would limit the growth of the front, so that this region would be unimportant. We believe that in experiments the growth of the front is dominated by the polydispersity of the particles. Extracting small additional effects will not be easy. In the simulations it is not clear from the evidence we have whether the growth is simply by heavier bolbs falling out of and so depleting the front or whether hydrodynamic diffusion is important. Away from the front we find a steady state, both in the experiments and the simulations. We believe from past experiments[8] that the velocity fluctuations will be independent of the size of the container if it is wide enough, whereas the variance grows linearly with the size in the simulations. We speculate that the nature of the experimental mixing is not the initial random positioning of the particles of the simulations but something yet to be quantified.

ACKNOWLEDGMENTS

We wish to thank O. Cardoso for the use of his PIV application and F. Ratouchniak for technical assistance.

[1] G. K. Batchelor, ''Sedimentation in a dilute dispersion of spheres,'' J. Fluid Mech. **52**, 245 (1972).
[2] R. E. Caflisch and J. H. C. Luke, ''Variance in the sedimenting speed of a suspension,'' Phys. Fluids **28**, 759 (1985).
[3] E. J. Hinch, ''Sedimentation of small particles,'' in *Disorder and Mixing*, edited by E. Guyon, J.-P. Nadal, and Y. Pomeau (Kluwer Academic, Dordrecht, 1988), p. 153.
[4] D. L. Koch, ''Hydrodynamic diffusion in a suspension of sedimenting point particles with periodic boundary conditions,'' Phys. Fluids **6**, 2894 (1994).
[5] F. R. Cunha, ''Hydrodynamic dispersion,'' Ph.D. thesis, Cambridge University, 1995.
[6] A. J. C. Ladd, ''Sedimentation of homogeneous suspensions of non-Brownian spheres,'' Phys. Fluids **9**, 491 (1997).
[7] F. R. Cunha, G. C. Abade, A. J. Sousa, and E. J. Hinch, ''Modeling and direct simulation of velocity fluctuations and particle-velocity correlations in sedimentation,'' J. Fluids Eng. **124**, 957 (2002).
[8] H. Nicolai and E. Guazzelli, ''Effect of the vessel size on the hydrodynamic diffusion of sedimenting spheres,'' Phys. Fluids **7**, 3 (1995).
[9] P. N. Segrè, E. Helbolzheimer, and P. M. Chaikin, ''Long-range correlations in sedimentation,'' Phys. Rev. Lett. **79**, 2574 (1997).
[10] G. Bernard-Michel, A. Monavon, D. Lhuillier, D. Abdo, and H. Simon, ''Particle velocity fluctuations and correlation lengths in dilute sedimenting suspensions,'' Phys. Fluids **14**, 2339 (2002).
[11] É. Guazzelli, ''Evolution of particle-velocity correlations in sedimentation,'' Phys. Fluids **13**, 1537 (2001).
[12] D. L. Koch and E. S. G. Shaqfeh, ''Screening mechanisms in sedimenting suspension,'' J. Fluid Mech. **224**, 275 (1991).
[13] A. Levine, S. Ramaswamy, E. Frey, and R. Bruinsma, ''Screened and unscreened phases in sedimenting suspensions,'' Phys. Rev. Lett. **81**, 5944 (1998).
[14] P. Tong and B. J. Ackerson, ''Analogies between colloidal sedimentation and turbulent convection at high Prandtl numbers,'' Phys. Rev. E **58**, R6931 (1998).
[15] M. P. Brenner, ''Screening mechanisms in sedimentation,'' Phys. Fluids **11**, 754 (1999).
[16] J. H. C. Luke, ''Decay of velocity fluctuations in a stably stratified suspension,'' Phys. Fluids **12**, 1619 (2000).
[17] A. J. C. Ladd, ''Effect of container walls on the velocity fluctuations of sedimenting spheres,'' Phys. Rev. Lett. **88**, 048301 (2002).
[18] S.-Y. Tee, P. J. Mucha, L. Cipelletti, S. Manley, M. P. Brenner, P. N. Segrè, and D. A. Weitz, ''Nonuniversal velocity fluctuations of sedimenting particles,'' Phys. Rev. Lett. **89**, 054501 (2002).
[19] P. J. Mucha and M. P. Brenner, ''Diffusivities and front propagation in sedimentation,'' Phys. Fluids **15**, 1305 (2003).
[20] R. H. Davis and M. A. Hassen, ''Spreading of the interface at the top of a slightly polydisperse sedimenting suspension,'' J. Fluid Mech. **196**, 107 (1988); ''Corrigendum,'' *ibid.* **202**, 598 (1989).
[21] S. Lee, Y. Jang, C. Choi, and T. Lee, ''Combined effect of sedimentation velocity fluctuation and self-sharpening on interface broadening,'' Phys. Fluids A **4**, 2601 (1992).
[22] J. Martin, N. Rakotomalala, and D. Salin, ''Hydrodynamic dispersion broadening of a sedimentation front,'' Phys. Fluids **6**, 3215 (1994).
[23] C. F. Bohren and D. R. Huffman, *Absorption and Scattering of Light by Small Particles* (Wiley-Interscience, New-York, 1983).
[24] O. Cardoso, D. Marteau, and P. Tabeling, ''Quantitative experimental study of the free decay of quasi-two-dimensional turbulence,'' Phys. Rev. E **49**, 454 (1994).